Lawrence Berkeley National Laboratory
LBL Publications

Title

Hartmann characterization of the PEEM-3 aberration-corrected X-ray photoemission electron microscope

Permalink
https://escholarship.org/uc/item/9rf031pn

Authors
Scholl, A
Marcus, MA
Doran, A
et al.

Publication Date
2018-05-01

DOI
10.1016/j.ultramic.2018.03.010

Peer reviewed

eScholarship.org Powered by the California Digital Library
University of California

Hartmann characterization of the PEEM-3 aberration-corrected X-ray Photoemission Electron Microscope

A. Scholl[1], M.A. Marcus[1], A. Doran[1], J.R. Nasiatka[1], A.T. Young[1], A.A. MacDowell[1], R. Streubel[2], N. Kent[2,3], J. Feng[1], W. Wan[1], H.A. Padmore[1]

[1]Advanced Light Source, Lawrence Berkeley National Laboratory, 1 Cyclotron Road, Berkeley CA 94720, USA

[2]Materials Sciences Division, Lawrence Berkeley National Laboratory, 1 Cyclotron Road, Berkeley CA 94720, USA

[3]Physics Department, UC Santa Cruz, Santa Cruz CA 95064, USA

Abstract

Aberration correction by an electron mirror dramatically improves the spatial resolution and transmission of photoemission electron microscopes. We will review the performance of the recently installed aberration corrector of the X-ray Photoemission Electron Microscope PEEM-3 and show a large improvement in the efficiency of the electron optics. Hartmann testing is introduced as a quantitative method to measure the geometrical aberrations of a cathode lens electron microscope. We find that aberration correction leads to an order of magnitude reduction of the spherical aberrations, suggesting that a spatial resolution of below 100 nm is possible at 100% transmission of the optics when using x-rays. We demonstrate this improved performance by imaging test patterns employing element and magnetic contrast.

1 Introduction

X-ray photoemission electron microscopy (X-PEEM) is a synchrotron based technique that allows researchers to image the morphology and the magnetic and chemical properties of surfaces, artificially grown thin films and minerals with nanometer-scale spatial resolution. X-PEEM has led to striking scientific discoveries in the area of materials sciences and physics, e.g., the observation of nanoscale domains in antiferromagnetic oxides[1] and the detection of the picosecond dynamics of magnetic vortex cores[2]. X-PEEM is an x-ray spectromicroscopy technique, combining spectroscopic sensitivity via the near edge x-ray absorption fine structure (NEXAFS) effect with lateral resolution provided by electron microscopy[3, 4]. In an X-PEEM instrument monochromatic x-rays from a synchrotron illuminate the sample and photoelectrons and secondary electrons are collected and imaged by the electron optics. The sample acts as a cathode, and the emitted electrons are accelerated rapidly towards the objective lens by an electrical field of 15-20 kV over about 2 mm. The spatial resolution of X-PEEM microscopes is usually reported to be near 20 nm[5, 6], but is in practice often in the 50-100 nm range for objects with weak contrast. Compared to other cathode lens techniques the relatively poor resolution is a consequence of the wide energy and transverse momentum distributions of the emitted electrons, resulting in blur caused by the chromatic and spherical aberrations of the microscope lenses. To reach high resolution, small contrast apertures need to be inserted that reduce the contribution of off-axis electrons but also drastically lower the transmission of the microscope. This leads to long exposure times and potentially higher radiation damage of sensitive samples. Increasing the photon flux to compensate for the inefficient microscope optics can lead to increased space charge blurring of images, further reducing the resolution.

Various approaches have been tried to reduce the impact of spherical and chromatic aberrations, for example the use of a dynamic correcting lens[7], coating the sample with diamondoid nanoclusters acting as an energy filter[8], or, as discussed here, the correction of the lowest order chromatic and spherical aberrations of the objective lens and accelerating field by an electron mirror[9-11]. The latter method has found broader use and has led to a spectacular improvement of the ultimate resolution of low energy electron microscopes (LEEMs) and UV-PEEMs using ultraviolet excitation. For X-PEEM's the progress has been slower but first experiments showed improved resolution but also a strong sensitivity to space charge effects[12]. We will discuss commissioning results of the aberration corrector of the PEEM-3 microscope, which is located at beamline 11.0.1 at the Advanced Light Source (ALS), a soft x-ray undulator beamline with variable polarization.

2.1 Experimental setup

Aberration correction of cathode lens electron microscopes is based on concepts developed by Rose[13] and Rempfer[14]. The ALS PEEM-3 microscope uses a tetrode mirror to correct 3rd order spherical and 1st order 1st degree (axial) chromatic aberrations[15, 16], Fig. 1. Electron optics, sample manipulator and 90° beam separator magnet rest on an in-vacuum optical table. A kinematically mounted rail system precisely positions the optical elements. The 5-axis sample

manipulator (x, y, z and two tilt axes) uses in-vacuum, piezo-driven linear stages and a flexure mechanism. Synchrotron x-rays illuminate the sample at an angle of 30 degrees to the sample surface. Samples can be cooled down to 30 K using liquid He cooling and heated up to 900 K using resistive or e-beam heating[17]. Current pulses, voltage pulses, in-situ electromagnetic fields, and in-situ rotation are deployed via special sample holders. All optical elements except for the separator magnet are electrostatic. This minimizes magnetic fields near the sample and prevents heating of the internal support structure. The optical table is fully enclosed inside a mu-metal box. A 1k x 1k pixel charged coupled device (CCD), fiber-coupled to an electron sensitive phosphor, is used for electron detection.

While using PEEM-3 in straight-through mode or ST-mode, the beam separator magnet is first demagnetized by applying an alternating field of decreasing amplitude. The magnified image of the sample formed by the objective lens is relayed by two round lenses across the demagnetized magnet and further relayed by a transfer lens. An aperture strip with several selectable back focal plane apertures (BFPAs) is located behind the transfer lens. The BFPA blocks off-axis electrons and improves the spatial resolution at the cost of microscope transmission. A projector optics group consisting of three lenses magnifies the image onto the CCD. A 12-pole electrostatic deflector assembly directly following the objective lens corrects stigmatic errors, and a set of quadrupoles at the exit of the beam separator steers the beam through the center of the transfer lens.

In aberration-corrected mode or AC-mode, the separator magnet is turned on and bends the electron beam twice, first by 90° towards the electron mirror and then again by 90° towards the CCD. The separator magnet assembly consists of a dipole magnet and three groups of optics consisting of a round lens plus two quadrupoles, which together provide astigmatic focusing at 1:1 magnification in each quadrant. This simple and tunable design is described in [18]. Diagnostic paddles with slits, pin holes and a TEM grid are located at image planes at the objective-side entrance and the mirror-side exit of the separator assembly. Each quadrant of the separator is chromatic but dispersion is cancelled after the 2nd pass through the magnet following inversion of the image by the mirror. Field lenses near image planes on the objective and mirror side of the separator magnet place a back focal plane in the mirror and remove field aberrations. Stigmatic errors of the objective lens are corrected by a 12-pole deflector near the objective lens. Likewise stigmatic errors of the mirror are corrected by a similar 12-pole deflector near the mirror. The mirror-side 12-pole deflector and a set of quadrupoles near the separator magnet are also used to correctly steer the beam towards the center of the mirror and along the center axis of the separator magnet. Transfer lens, back focal plane apertures and projector lenses are used for resolution improvement and magnification.

The electron mirror was designed to guarantee micron-scale accuracy in the mechanical registration of the electrodes. Phosphor bronze blanks were first mechanically cut and critical surfaces were then diamond-turned to high precision and an optical finish. Concentric registration and electrical isolation of the electrodes was achieved using a chain of sapphire

balls placed in concentric grooves, distributing the mechanical forces within the spring-loaded assembly. A cylindrical metal can shields the internal electrodes and supports the mirror on the in-vacuum rail system. The PEEM-3 mirror with three adjustable electrode potentials is capable of canceling lowest order spherical and chromatic aberrations at a constant imaging distance for a wide range of operating conditions of the microscope. Aberration correction coefficients of the mirror were computed as function of electrode voltage at constant focal length of the mirror and the generated set of correction voltages was then fitted using 5th order polynomial surfaces as function of two free parameters: CC (chromatic correction parameter), CS (spherical correction parameter)[16]. The CC and CS correction values can thus be easily adjusted to tune the aberration correction. A small offset voltage applied to the last mirror electrode is being used to tweak the focal length of the mirror.

2.2 Hartmann measurement of aberration coefficients

Geometric aberrations, in particular spherical aberrations, limit the performance of X-PEEM. Electrons created by the absorption of high-energy x-rays start from the sample with non-zero energy and a wide angular distribution. First order aberrations, defocus and astigmatism, can be easily countered by adjusting lens voltages and using multipole deflectors. Second order aberrations vanish in a cylinder-symmetrical system and, if present, need to be removed by proper alignment of the electron beam in the microscope. Third order spherical aberrations and axial chromatic aberrations cannot be removed by round electron optics and need to be compensated by the electron mirror.

Approximate aberration coefficients of the frontend optics have been computed for PEEM-3[16], but in practice we need to experimentally determine the frontend aberrations and find optimal mirror parameters. To this purpose we employ a method derived from the well-known Hartmann technique, which was developed historically for the optical metrology of large light optics, Fig. 2. Light from a point source passes through a hole screen, the Hartmann screen, and is then reflected by the test mirror and finally imaged by a detector near an image plane. Optics imperfections of the mirror warp the displayed dot pattern and the displacements versus the hole coordinate are then fitted by a series of weighted polynomials. A contemporary review of the Hartmann technique can be found in [19]. This technique is similar to the microspot LEED technique discussed in [20] but can also be used in PEEM mode. The Zernike polynomials $Z_n^m(r,\theta)$ are a commonly used basis for the fitting of optical aberrations and the Zernike coefficients provide quantitative information about the low order geometric aberrations of the tested optics[21, 22]. In case of PEEM-3, a 10-µm-size back focal plane aperture was scanned across the electron beam, allowing a narrow ray of electrons to pass to the detector. For each position of the BFPA we acquired an image of a test pattern and determined the pattern's location on the detector. Since we measured the image displacements x and y as function of aperture position X and Y and not the curvature of the wave front we used the derivatives D_i^X and D_i^Y of the Zernike polynomials versus X and Y as fit functions:

$$x(X,Y) = \sum Z_i D_i^X(X,Y)$$
$$D_3^X = 4X, D_4^X = 2Y, D_5^X = -2X,$$
$$D_6^X = 9X^2 + 3Y^2 - 2, D_7^X = 6XY,$$
$$D_8^X = 12X(2X^2 + 2Y^2 - 1)$$

A corresponding set of fit function was used to fit y(X,Y). The Zernike coefficients Z_3, Z_4, Z_5 are the 1st order defocus and the "x"-oriented and "+"-oriented astigmatisms, Z_6 and Z_7 are the 2nd order coma in X and Y direction and Z_8 is the 3rd order spherical aberration. The scan pattern of the back focal plane aperture is shown in Fig. 3a. Oversampling improved accuracy, and we measured the image displacement for 28 positions of the BFPA at three different distances from the optical axis to determine six Zernike coefficients, relying on a least square optimization method. We experimented with including higher order aberrations, in particular Z_9, Z_{10} (trefoil) and additional third order aberrations but did not observe a reduction in the residue and therefore an improved quality of the fit. Preceding and following the measurement along each circular track we recorded an image at zero BFPA displacement in order to subtract slow sample drift. Typical exposure times were two to ten seconds per image or a few minutes for a full Hartmann measurement. Fig. 3b) shows images of the test pattern for three 20 µm off-axis locations of the BFPA and for the BFPA positioned on the optical axis. Three images are relatively poorly resolved because of the large uncorrected aberrations for off-axis rays. Note that the displayed images were acquired in ST-mode with the aberration corrector turned off. To quantify the displacements we cross-correlated all images with the reference image at zero displacement and determined the shift of the pattern with a nominal accuracy of 1/4 of a pixel (1/4 of a pixel corresponds to ~2.5 nm). The same methods were used in ST-mode and in AC-mode but the scan pattern was scaled in size to account for the larger magnification of the optics at the BFPA position in AC-mode (Fig. S1). Fig. 3c) shows the measured and fitted contribution of the spherical aberration to the total image displacement for several CS correction values. These graphs are the result of the Hartmann fit and illustrate the magnitude of the Zernike coefficient Z_8. A minimal displacement for large BFPA offsets indicates a good correction of the spherical aberration near CS = -14500 m. CS is the dialed-in spherical aberration correction value of the mirror.

Fig. 4 compares the measured and fitted Hartmann displacements, which quantify the geometric image errors, broken up by order for ST-mode (a) and AC-mode (b). In ST-mode 3rd order aberrations dominate (displacements shown in the bottom right panel of Fig. 4a). Apparently, a non-zero defocus of opposite sign (top right panel) was chosen during microscope alignment so that it partially compensated the image blur due to spherical aberrations (compare the direction of the missing pie slice for 1st and 3rd order aberrations). 3rd order aberrations are much smaller in AC-mode and an optimal CS correction value of -14500 m was found (bottom right panel of Fig. 4b). The overall magnitude of the geometrical aberration caused displacements is also much smaller (black line, top left panel of 4b in comparison to 4a). 2nd order aberrations are small in ST and in AC mode, as expected for a well aligned optics. The

size of the residue of the fit (red dots) indicates that the remaining aberrations are smaller or of similar magnitude as the measurement error of the Hartmann method.

Repeating the optics alignment process following different recipes showed that 2nd order aberrations (coma) can become dominant in AC-mode, for example when the electron beam does not enter the mirror on axis. Proper alignment of the beam in lenses and especially in the mirror are therefore crucial to achieve a high performance of the aberration corrector. The described Hartmann method is able to differentiate between errors caused by an incorrect objective lens voltage (defocus), poor alignment (astigmatism and coma), and uncompensated spherical aberrations and provides an accurate method to qualify the optics of the aberration corrected X-PEEM microscope.

	1st order (nm/μm)	2nd order (nm/μm^2)	3rd order (nm/μm^3)	beam spread (nm)
ST-mode	0.58	0.013	0.00038	777
AC-mode	0.38	0.008	0.00004	82

Table 1: 1st to 3rd order aberration coefficients and contribution of the spherical aberration to the beam spread on the detector.

	1st order in μm/rad	2nd order in mm/rad^2	3rd order in m/rad^3
ST-mode	19	14	14
AC-mode	12	9	1.5

Table 2: 1st to 3rd order aberration coefficients and contribution of the spherical aberration to the beam spread on the detector as function of the beam angle at the transfer lens.

Table 1 lists the aggregated aberration coefficients by order for ST-mode and AC-mode. Same order aberrations (1st order: Z3-Z5, 2nd order: Z6-Z7, 3rd order: Z8) were added in quadrature. To take into account the 1.63 times larger magnification of AC-mode at the BFPA position (Fig. S1), the aberration coefficients for ST-mode were scaled by 1/1.63 in 1st order, $1/1.63^2$ in 2nd order and by $1/1.63^3$ in 3rd order. This allows us to compare ST-mode and AC-mode directly. We list the aberration coefficients in units of nm (image displacement) per μm^n (aperture displacement, n = 1,2,3 is the aberration order). We list the aberration coefficients as function of the beam angle at the transfer lens in table 2.

While the compounded 1st and 2nd order errors are of similar magnitude in ST- and AC-mode, we measure an order of magnitude reduced 3rd order coefficient, demonstrating the ability of the mirror corrector to cancel and suppress the effect of spherical aberrations. It is noteworthy that the mirror corrector does not increase other low order aberrations—they are in fact about 40% smaller in this experiment–which demonstrates the high quality of the mechanical and

optical alignment of the mirror arm optics. To put those values into context we compute and list the approximate displacement of electron rays passing the BFPA plane at a distance from the optical axis of 44 µm in AC-mode and 27 µm in ST-mode in the column labeled 'beam spread". These numbers represent the median beam radius: half of the electrons pass within a disc of this size, Fig. S1. The displacements are presented in object coordinates for a virtual magnification of the microscope of 1. They can be interpreted as the median radius of the aberrated image of a point source. As expected, spherical aberrations cause very large image errors of hundreds of nanometers in ST-mode. The beam spread at the detector extends over more than 700 nm, with 50% of the electrons landing outside a disc of this radius. Aberration correction reduces the spread at the detector due to spherical aberrations to less than 100 nm. This should allow us to achieve 100 nm level spatial resolution, even without the use of a back focal plane aperture and at 100% transmission of the electron optics, as predicted in [15]. It must be noted that we have not considered the effect of axial chromatic aberrations here, which can be large for an x-ray PEEM. The PEEM-3 electron mirror is expected to counter these as well, as images of test patterns will show.

2.3 Demonstration of aberration correction on test patterns

Fig. 5 shows X-PEEM images of an elbow-shaped line pattern, which were acquired using element contrast at the Ni edge without using a contrast-enhancing BFPA. The patterns were manufactured by e-beam lithography in Ni on a Si substrate[17]. The width of the lines was 150 nm and areas covered by Ni appeared bright. Images were exposed for 10 s and a sample voltage of 15 kV was used, which is a conservative value. For very high resolution experiments we typically operate PEEM-3 at up to 20 kV or even at higher sample voltages, resulting in an approximately proportional improvement in resolution and at the same time improved detector signal. The image brightness was similar in ST- and AC-mode, indicating that the microscope transmission in ST-mode and AC-mode were the same. However, we chose to insert an image plane aperture of 100 µm diameter in the objective lens column when using AC-mode in order to reduce the electron density at the electron turnaround point in the mirror and prevent space charge blurring, which was severe otherwise. This image plane aperture restricted the field of view to about 8 µm but did not lower the transmission of the microscope within the field of view. We observed that the image plane aperture upstream of separator magnet and mirror effectively eliminated space charge effects for low to moderate x-ray flux (see also Fig. S2). Intensity profiles across the pattern along the horizontal and the vertical direction show a 2-3 times reduced contrast without using aberration correction and a wide halo, while the AC-mode images look crisp and the Ni lines appear at higher contrast. The line intensity within the pattern is still below the intensity of areas far from the pattern, which means that electrons with large transverse momentum (high initial energy and large emission angle) are still not optimally focused, even using AC-mode. This is likely the result of higher order aberrations that are not corrected and possibly of not optimally chosen CC and CS correction values. In particular, choosing an optimal CC value is not straightforward when the

source is polychromatic and no energy filter is used. A range of CC values was tried and the images with best resolved features are shown here.

In order to quantify the relative contrast transfer of ST-mode and AC-mode we imaged a nano-magnet lattice of 2.8 nm thick Ni80Fe20 rectangular islands at the Fe L_3 edge, Fig. 6[23]. The islands are 470 x 170 nm in size on a lattice with 600 nm spacing. The islands appear bright, while the Si substrate appears dark. Uncorrected images (left column) are compared with aberration-corrected images (right column), while not using a BFPA (top row) and while using a contrast enhancing BFPA (bottom row). The 100 µm size image plane aperture upstream of the mirror is visible in the AC-mode images and was again used to prevent space charge blurring. For the high resolution images, small back focal plane apertures of 15 µm (ST-mode) and 20 µm (AC-mode) were chosen. The top row images illustrates the primary function of the mirror corrector in an X-PEEM at high transmission: The mirror removes the large diffuse background of badly aberrated, off-axis rays and dramatically increases the image contrast. The relative image contrast was determined using two methods, the first relied on measuring the variation of the image intensity along a line profile (dashed red line), the second was based on measuring the relative strength of the 2nd and 1st order reciprocal space spots of the periodic lattice in Fourier space. The amplitude of higher frequency components in Fourier space decreases with decreasing contrast transfer, therefore the intensity ratio of different order spots can be used to compare the optical quality of images of such a lattice structure. The inset in Fig. 6a shows the Fourier transform of a real space X-PEEM image with the 1st and 2nd order spots marked by red circles. The position of the 2nd order spot in Fourier space corresponds to a real space distance or line width of 106 nm.

The bar diagram in Fig. 6 b) lists the pattern to gap contrast along a row of nanomagnets for four tested X-PEEM modes. The data were normalized to the value measured using a 20 µm BFPA in AC-mode, which showed the highest contrast. In ST mode and using a BFPA the contrast is reduced to about 75%, it is about 55% at optimal microscope transmission when using AC-mode and no BFPA, and it is very low, around 15%, when using neither aberration correction nor a BFPA. We observe that aberration correction improves the image quality and contrast transfer considerably when no BFPA is used (15% to 55% relative contrast). This improvement is less striking but still visible (75% to 100% relative contrast) when inserting a BFPA, which by itself reduces the contribution of badly aberrated rays. A similar trend is visible in Fig. 6 c) which summarizes the Fourier space analysis. Fig. 6 c) shows a sizeable increase in the relative intensity of the 2nd order reciprocal space spot when the AC correction is turned on, with and without a BFPA. We have repeated this analysis using the 3rd order reciprocal space spot and obtained similar results. According to these measurements AC-mode without a BFPA is even competitive with ST-mode using a small BFPA. In summary, both analysis methods reveal a large improvement in image contrast at high microscope transmission and a smaller but still measureable improvement at low transmission, when a BFPA is used.

We also studied the performance of the aberration correction in magnetic microscopy experiments. Fig. 7 shows x-ray magnetic circular dichroism (XMCD) images of an array of 100 nm diameter magnetic islands on a 150 nm period honey comb lattice[24]. The distance between the 10 nm thick $Ni_{80}Fe_{20}$ discs is 50 nm. Magnetic imaging of such disc patterns is challenging because the magnetic contrast is around 10 times weaker than the element contrast employed in the previous tests and the distance between the islands is small and approaches the resolution limit of PEEM-3. Ten images were acquired at the Fe L_3 edge at 707 eV for each circular x-ray polarization, averaged, and then divided. The resulting XMCD images are shown at the same level of contrast using ST-mode on the left, using AC-mode on the right, without using a BFPA in the top row and using BFPAs to improve contrast at the cost of transmission in the bottom row. The transmission without using a BFPA is nominally 100%, while it is reduced to 14% using a 20 µm diameter aperture in ST-mode and to 28% using a larger, 50 µm aperture in AC-mode. The magnetic patterns are well resolved in both AC-mode and ST-mode when using a BFPA but a twice larger transmission can be chosen when the aberration correction is employed. Even without a contrast enhancing BFPA in use, aberration corrected images have sufficient quality for analysis while the uncorrected images are of poor quality and have very low contrast. The total exposure time needed to measure the aberration corrected domain image in high transmission mode (no BFPA) was 10s per polarization (1s per exposure) at a field of view of 8 µm and at about 30 % of the maximal available x-ray flux. The images demonstrate that aberration correction enables imaging of features with sub 100 nm scale separation at higher transmission of the electron optics. Short exposure times become possible even when operating at very high magnification.

3 Conclusions

We have shown that aberration correction significantly improves the resolution of the PEEM-3 electron optics, in particular, when a high microscope transmission and efficiency are needed, e.g., for fast (dynamic) imaging or to prevent x-ray damage. Hartmann measurements show that spherical aberrations, which are massive for off-axis electrons in an uncorrected PEEM, are reduced by an order of magnitude. Demonstration measurements on samples that cover important use cases of the instrument show that chromatic and spherical aberrations are well cancelled by the electron mirror and allow us to image 100 nm scale and smaller features with good contrast and low background even at high transmission. The mirror does not increase other low order geometrical aberrations, proving the good alignment of the optics. We have shown that Hartmann measurements are critical for tuning the microscope and for qualifying the optics of an X-PEEM.

Acknowledgments

This research used resources of the Advanced Light Source, which is a DOE Office of Science User Facility under contract no. DE-AC02-05CH11231. R.S. and N.K. acknowledge support from the U.S. Department of Energy, Office of Science, Basic Energy Sciences, Materials Sciences and Engineering Division under Contract No. DE-AC02-05-CH11231 (NEMM program MSMAG). The magnetic lattice samples were prepared by J.D. Watts, A.M. Albrecht and C. Leighton at the

University of Minnesota and Y. Lao and J. Sklenar at the University of Illinois. We would like to thank D. Deboer and B. Conners for the fabrication and mechanical alignment of the electron optics of the mirror corrector. The elbow test pattern was produced by W. Chao and E. Anderson at the LBNL Center for X-ray Optics.

Figures

Fig. 1: Layout of the PEEM-3 microscope. The photo shows a view from the mirror towards the separator magnet assembly.

Fig. 2: Classical Hartmann arrangement for the evaluation of large light optics[19].

Fig. 3: a) Scan pattern of the back focal plane aperture to determine 1st, 2nd and 3rd order geometrical aberrations. b) Images showing a test pattern and its displacement (dashed lines) for four select aperture positions (#1, #26, #27, #20). c) Contribution by 3rd order (spherical) aberrations to the Hartmann displacements x and y for three different CS correction values in AC-mode.

Fig. 4: a) Hartmann displacement for PEEM-3 operating in straight-through, ST-mode shown in total and broken up by the order of geometrical aberration. The residual of the fit is also shown. b) The same for aberration-corrected, AC-mode demonstrating the substantial reduction of the 3rd order (spherical) aberration. The measured displacements are in black, the fitted displacements by order are in blue and the residue of the fit is shown as red dots.

Fig. 5: 150 nm line width, elbow-shaped lithographic patterns imaged using a) ST-mode" and b) AC-mode at 100% transmission (back focal plane aperture removed). c) Line profiles across the vertical and horizontal lines.

Fig. 6: a) Nanomagnet array imaged at the Fe L_3 edge, using ST-mode (left column) and AC-mode (right column). The top row shows images taken at full transmission without using a back focal plane aperture, images in the bottom row were acquired using a 15 µm aperture in ST-mode and a 20 µm aperture in AC-mode for optimum spatial resolution. The same contrast enhancement was used. The inset shows the amplitude of the discrete Fourier transform. The 1st and 2nd order reciprocal space spots of the pattern are marked. b) Pattern contrast measured along a line profile (red dashed line). c) Contrast transfer measured as the ratio of the 2nd to 1st order diffraction spot.

Fig. 7: XMCD images of a honey comb pattern of 100 nm sized circular magnetic islands imaged using (left) ST-mode and (right) AC-mode. The percentages quantify the transmission of the microscope for the selected back focal plane apertures. The same contrast enhancement was used when displaying the images.

References

[1] A. Scholl, J. Stöhr, J. Lüning, J. W. Seo, J. Fompeyrine, H. Siegwart, J. P. Locquet, F. Nolting, S. Anders, E. E. Fullerton, M. R. Scheinfein, and H. A. Padmore, "Observation of antiferromagnetic domains in epitaxial thin films," *Science*, vol. 287, pp. 1014-16, 2000.

[2] S. B. Choe, Y. Acremann, A. Scholl, A. Bauer, A. Doran, J. Stohr, and H. A. Padmore, "Vortex core-driven magnetization dynamics," *Science*, vol. 304, pp. 420-2, 2004.

[3] T. Schmidt, S. Heun, J. Slezak, J. Diaz, K. C. Prince, G. Lilienkamp, and E. Bauer, "SPELEEM: Combining LEEM and spectroscopic imaging," *Surface Review and Letters*, vol. 5, pp. 1287-1296, 1998.

[4] J. Stöhr, Y. Wu, B. D. Hermsmeier, M. G. Samant, G. R. Harp, S. Koranda, D. Dunham, and B. P. Tonner, "Element-specific magnetic microscopy with circularly polarized X-rays," *Science*, vol. 259, pp. 658-61, 1993.

[5] S. Anders, H. A. Padmore, R. M. Duarte, T. Renner, T. Stammler, A. Scholl, M. R. Scheinfein, J. Stöhr, L. Seve, and B. Sinkovic, "Photoemission electron microscope for the study of magnetic materials," *Review of Scientific Instruments*, vol. 70, pp. 3973-81, 1999.

[6] G. De Stasio, L. Perfetti, B. Gilbert, O. Fauchoux, M. Capozi, P. Perfetti, G. Margaritondo, and B. P. Tonner, "MEPHISTO spectromicroscope reaches 20 nm lateral resolution," *Review of Scientific Instruments*, vol. 70, pp. 1740-1742, 1999.

[7] G. Schönhense and H. Spiecker, "Correction of chromatic and spherical aberration in electron microscopy utilizing the time structure of pulsed excitation sources," *Journal of Vacuum Science & Technology B*, vol. 20, pp. 2526-34, 2002.

[8] H. Ishiwata, Y. Acremann, A. Scholl, E. Rotenberg, O. Hellwig, E. Dobisz, A. Doran, B. Tkachenko, A. Fokin, P. Schreiner, J. Dahl, R. Carlson, N. Melosh, Z. Shen, and H. Ohldag, "Diamondoid coating enables disruptive approach for chemical and magnetic imaging with 10 nm spatial resolution," *Applied Physics Letters*, vol. 101, 2012.

[9] T. Schmidt, U. Groh, R. Fink, and E. Umbach, "XPEEM with energy-filtering: Advantages and first results from the smart project," *Surface Review and Letters*, vol. 9, pp. 223-232, 2002.

[10] R. M. Tromp, J. B. Hannon, W. Wan, A. Berghaus, and O. Schaff, "A new aberration-corrected, energy-filtered LEEM/PEEM instrument II. Operation and results," *Ultramicroscopy*, vol. 127, pp. 25-39, 2013.

[11] R. Konenkamp, R. C. Word, G. F. Rempfer, T. Dixon, L. Almaraz, and T. Jones, "5.4 nm spatial resolution in biological photoemission electron microscopy," *Ultramicroscopy*, vol. 110, pp. 899-902, 2010.

[12] T. Schmidt, A. Sala, H. Marchetto, E. Umbach, and H. J. Freund, "First experimental proof for aberration correction in XPEEM: Resolution, transmission enhancement, and limitation by space charge effects," *Ultramicroscopy*, vol. 126, pp. 23-32, 2013.

[13] M. Haider, H. Rose, S. Uhlemann, B. Kabius, and K. Urban, "Towards 0.1 nm resolution with the first spherically corrected transmission electron microscope," *Journal of Electron Microscopy*, vol. 47, pp. 395-405, 1998.

[14] G. F. Rempfer, D. M. Desloge, W. P. Skoczylas, and O. H. Griffith, "Simultaneous correction of spherical and chromatic aberrations with an electron mirror: An electron optical achromat," *Microscopy and Microanalysis*, vol. 3, pp. 14-27, 1997.

[15] J. Feng, E. Forest, A. A. MacDowell, M. Marcus, H. Padmore, S. Raoux, D. Robin, A. Scholl, R. Schlueter, P. Schmid, J. Stohr, W. Wan, D. H. Wei, and Y. Wu, "An x-ray photoemission electron microscope using an electron mirror aberration corrector for the study of complex materials," *Journal of Physics-Condensed Matter*, vol. 17, pp. S1339-S1350, 2005.

[16] W. Wan, J. Feng, H. A. Padmore, and D. S. Robin, "Simulation of a mirror corrector for PEEM3," *Nuclear Instruments & Methods in Physics Research Section A*, vol. 519, pp. 222, 2004.

[17] A. Doran, M. Church, T. Miller, G. Morrison, A. T. Young, and A. Scholl, "Cryogenic PEEM at the Advanced Light Source," *Journal of Electron Spectroscopy and Related Phenomena*, vol. 185, pp. 340-346, 2012.

[18] W. Wan, J. Feng, and H. A. Padmore, "A new separator design for aberration corrected photoemission electron microscopes," *Nuclear Instruments & Methods in Physics Research Section a-Accelerators Spectrometers Detectors and Associated Equipment*, vol. 564, pp. 537-543, 2006.

[19] D. Malacara-Hernandez and D. Malacara-Doblado, "What is a Hartmann test?," *Applied Optics*, vol. 54, pp. 2296-2301, 2015.

[20] R. M. Tromp, "Characterization of the cathode objective lens by Real-Space Microspot Low Energy Electron Diffraction," *Ultramicroscopy*, vol. 130, pp. 2-6, 2013.

[21] V. Lakshminarayanan and A. Fleck, "Zernike polynomials: a guide," *Journal of Modern Optics*, vol. 58, pp. 545-561, 2011.

[22] F. Zernike, "Diffraction theory of the knife-edge test and its improved form, the phase-contrast method.," *Monthly Notices of the Royal Astronomical Society*, vol. 94, pp. 0377-0384, 1933.

[23] I. Gilbert, Y. Y. Lao, I. Carrasquillo, L. O'Brien, J. D. Watts, M. Manno, C. Leighton, A. Scholl, C. Nisoli, and P. Schiffer, "Emergent reduced dimensionality by vertex frustration in artificial spin ice," *Nature Physics*, vol. 12, pp. 162-+, 2016.

[24] S. Velten, R. Streubel, A. Farhan, N. Kent, M. Y. Im, A. Scholl, S. Dhuey, C. Behncke, G. Meier, and P. Fischer, "Vortex circulation patterns in planar microdisk arrays (vol 111, 059901, 2017)," *Applied Physics Letters*, vol. 111, 2017.

Supplemental information

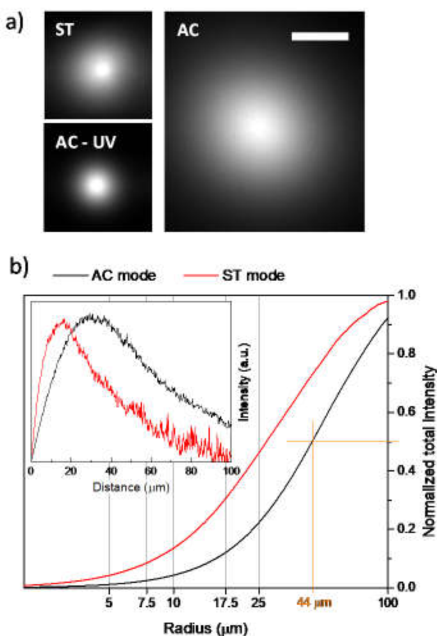

Fig. S1: a) Electron distribution at the BFP-aperture position imaged using the PEEM-3 projector optics for the “straight-through” imaging mode using x-rays (ST), aberration-corrected, “aberration corrected” imaging mode using x-rays (AC), and aberration-corrected imaging using UV (AC-UV). The length of the scale bar is 10 µm. b) Microscope transmission as function of assumed aperture radius for aberration-corrected and straight-through mode in the case of using x-rays. The beam median radius (half of the electrons are within this radius) is shown in orange. The inset shows the circularly integrated intensity as function of distance from the electron beam center.

The magnification of the microscope frontend changes between (straight through) ST-mode and (aberration corrected) AC-mode. We have measured the electron beam profile at the (back focal plane aperture) BFPA position by choosing a special operation mode of the projector column that is designed to image the back focal plane onto the CCD detector, Fig. S1. The image magnification was measured by overlaying the shadow image of a BFPA of known size and measuring its diameter in detector pixel. The median radius of the electron beam was 44 µm in AC-mode and 27 µm in ST-mode, corresponding to a 1.63 times larger magnification of the AC-mode at the BFPA position. The electron intensities as function of position from the beam axis are also shown, first integrated from the center of the beam to a given distance and secondly (inset) integrated along a circle of a given radius. The electron beam diameter at the BFPA for ultraviolet (UV) illumination is considerably smaller. The UV light of a mercury arc lamp excites electrons very close to the workfunction cutoff and the range of possible transverse momenta is much lower, resulting in a narrower beam at the BFPA position. This reduces the effect of spherical and chromatic aberrations using UV light compared to x-rays, and leads to the typically higher spatial resolution of UV-PEEM images.

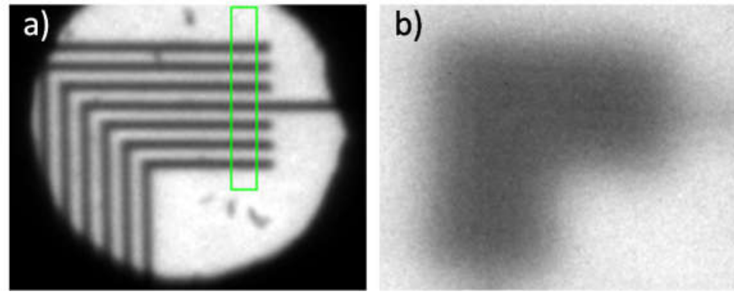

Fig. S2: Images of an elbow test pattern in AC-mode at high x-ray flux. An image plane aperture was used in image a) to reduce the electron density in the electron mirror, no image plane aperture was used in b). The green box marks an area that was used for a quantitative analysis of the line pattern contrast.

We illustrate the effect of space charge by comparing two aberration corrected images using similar imaging conditions where the first was taking after radically reducing the electron flux in the mirror by inserting a small image plane aperture in the objective column, Fig. S2. Because this aperture is at an image plane, it is conjugate to the sample plane. It therefore does not reduce the microscope transmission for rays coming from points within a 4 µm area of the sample but blocks electrons coming from elsewhere, ultimately reducing the total number of electrons that reach the mirror. Both images were acquired using AC-mode and with a 35 µm BFPA in place. Moderate x-ray flux and a 50 µm size image plane aperture upstream of the mirror was used in S2a) while no aperture and an increased x-ray flux was used in S2b). The frontend magnification is about 12, relating the diameter of the image plane aperture to the diameter of the visible area of the sample. The space charge blurred image b) is of very poor quality. The relatively low duty cycle of synchrotron x-rays–the ALS produces 80 ps pulses every 2 ns–results in a relatively high peak electron flux in the microscope compared to that produced by constant wave (CW) sources at the same time averaged flux, e.g., by arc lamps or electron guns. This low duty cycle causes an increased sensitivity to space charge effects in the mirror, especially near the turnaround point where electrons come to rest before they are accelerated back towards the separator. Space charge effects near the sample appear to be of lesser importance, probably because of the large gradient of the accelerating electric potential. We only observe sample localized space charge effects at the ALS PEEM-3 during the so-called 2-bunch mode, which is a special operation mode of the synchrotron with about 10x increased x-ray peak fluence. In case of PEEM-3, space charge blurring can be severe but can also be effectively managed by reducing the field of view through an image plane aperture. This method was employed throughout this work.

Manipulator

Sample

X-rays

Separator magnet

SL+Q

Back focal plane aperture

OL

FL

DP

DP

FL

TL

PL

PL

PL

DP

Mirror

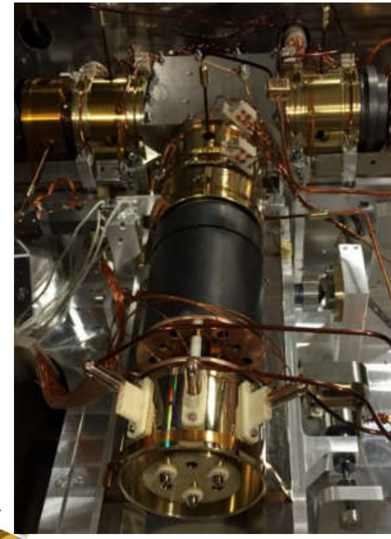

OL: objective lens

FL: field lens

DP: diagnostic paddle

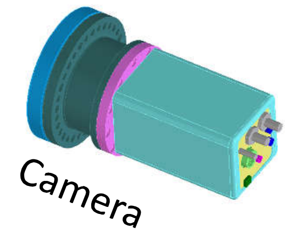

Camera

TL: transfer lens

PL: projector lens

SL+Q: separator lens/quadrupoles

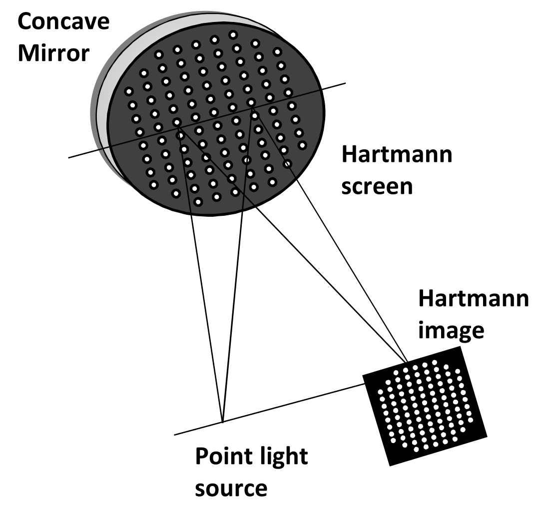
Concave
Mirror
Hartmann
screen
Hartmann
image
Point light
source

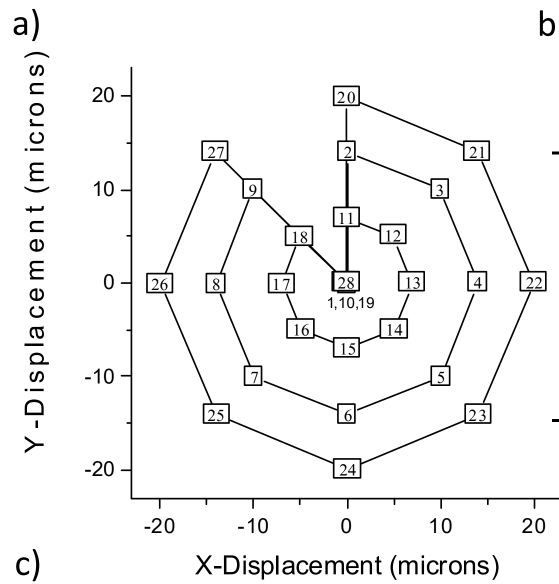
a)
Y-Displacement (microns)
X-Displacement (microns)
1,10,19
20
-20
10
-10
0

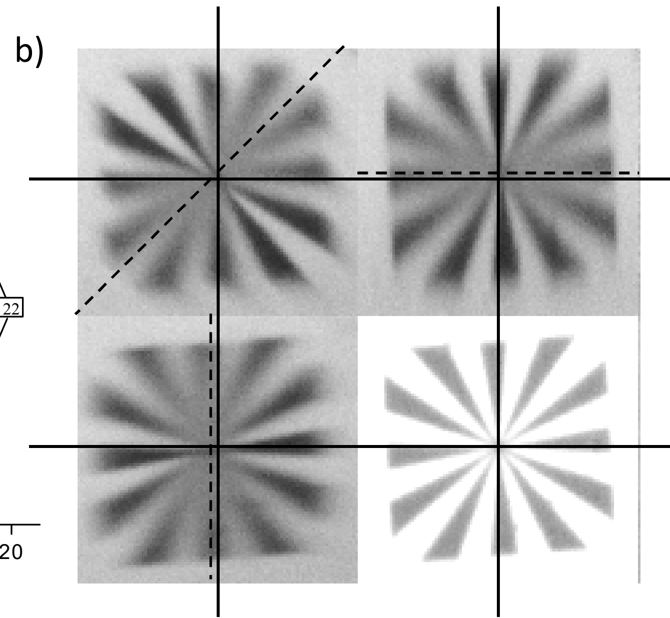
b)

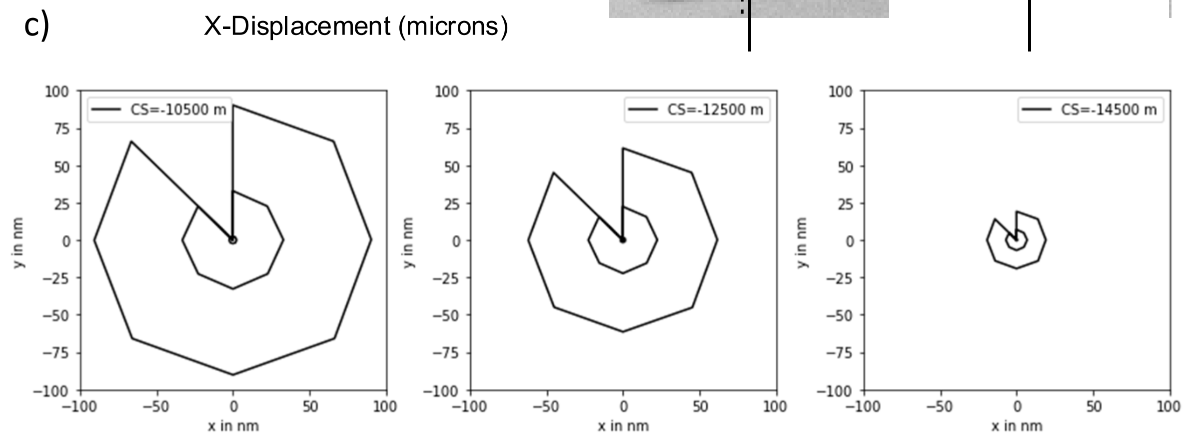
c)
CS=-10500 m
CS=-12500 m
CS=-14500 m
y in nm
x in nm

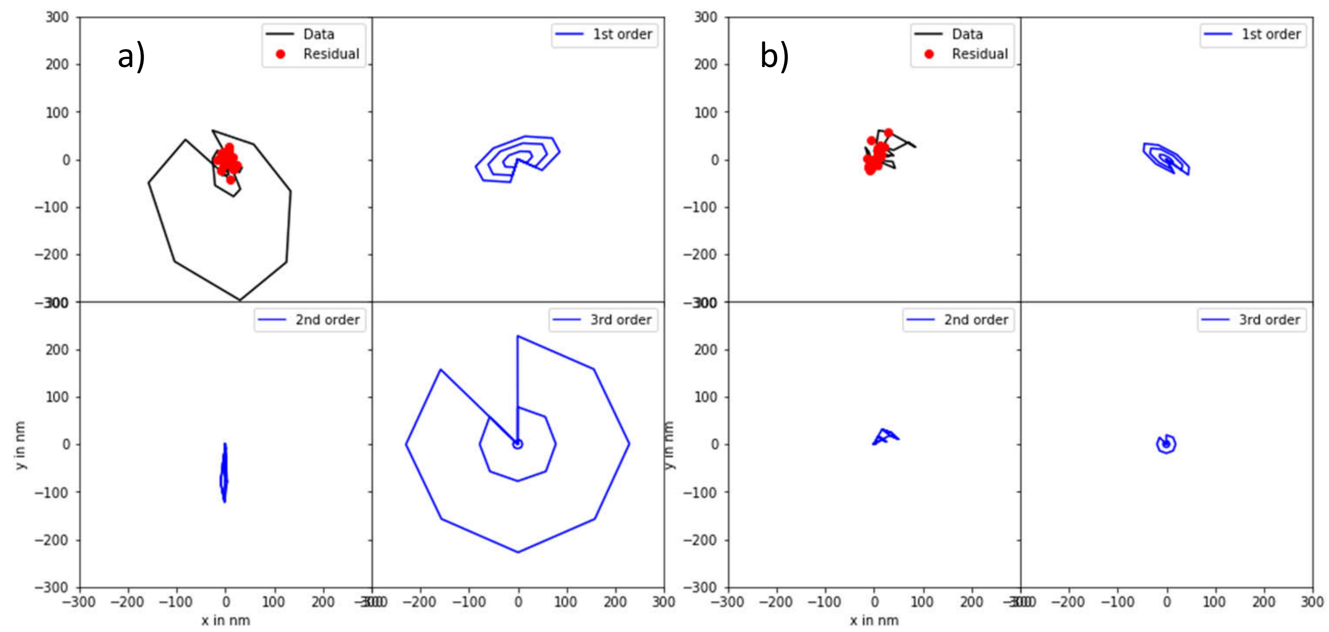
a)
Data
Residual
1st order
2nd order
3rd order
b)
y in nm
x in nm

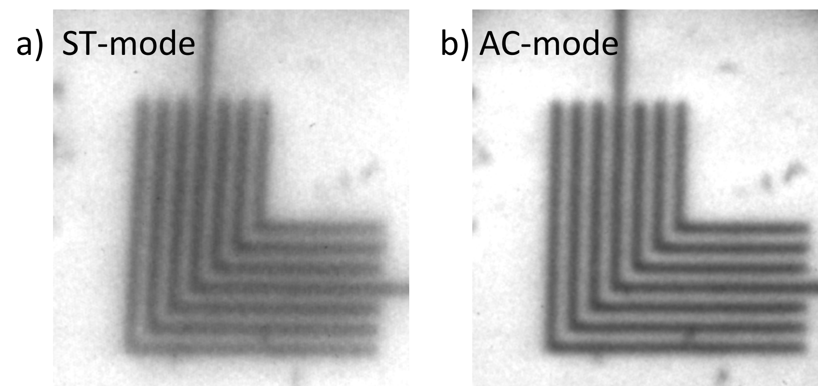
a) ST-mode
b) AC-mode

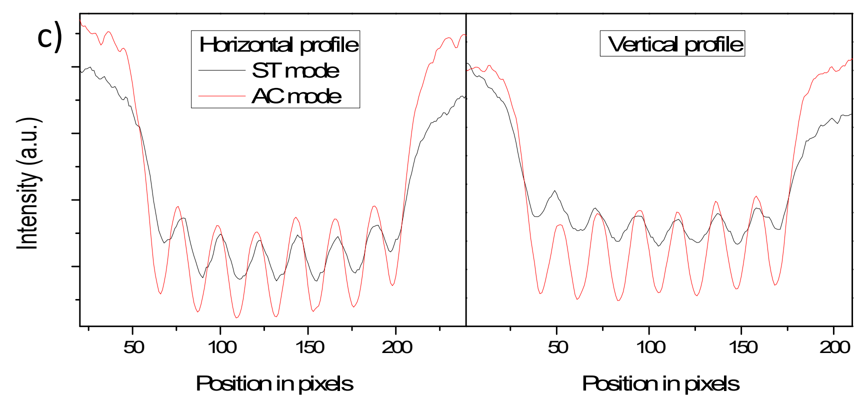
c)
Horizontal profile
ST mode
AC mode
Vertical profile
Intensity (a.u.)
50
100
150
200
Position in pixels
50
100
150
200
Position in pixels

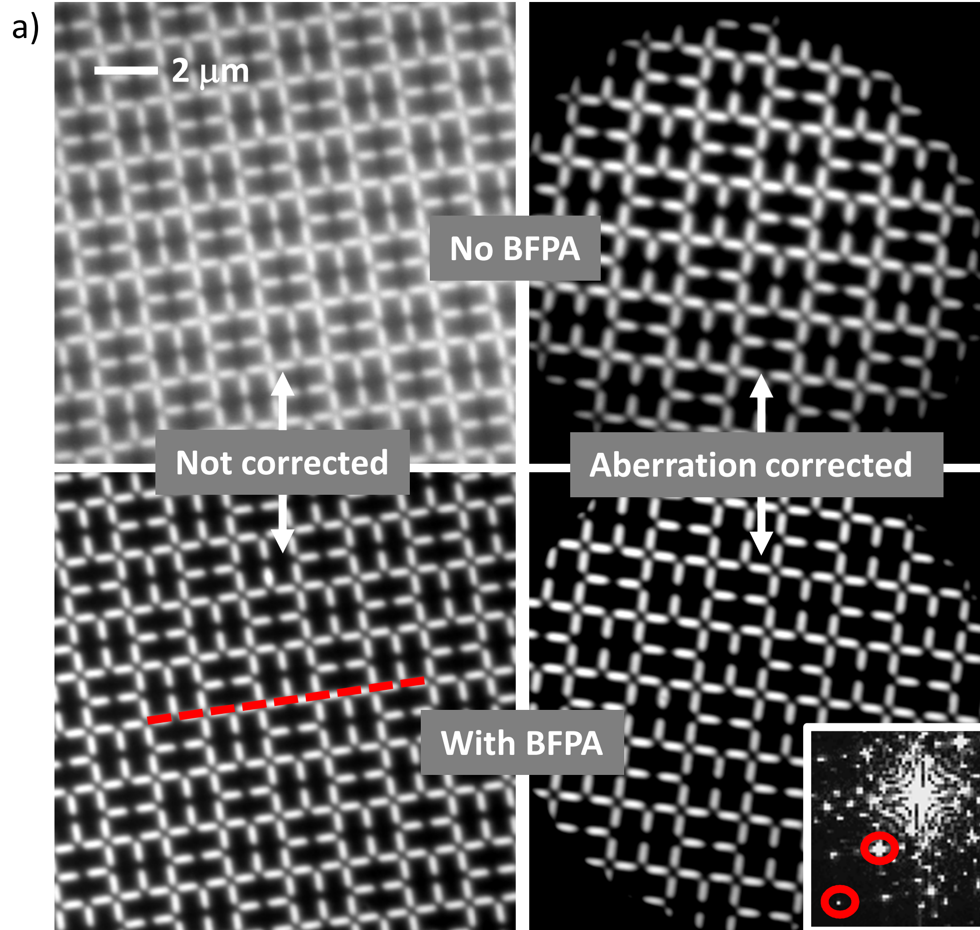
a)
2 μm
No BFPA
Not corrected
Aberration corrected
With BFPA

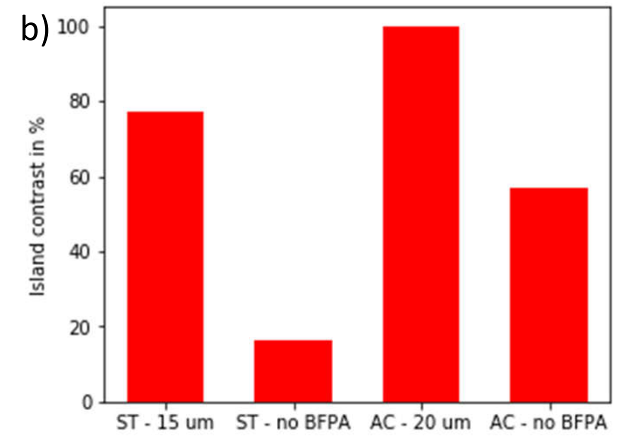
b)
Island contrast in %
100
80
60
40
20
0
ST - 15 um
ST - no BFPA
AC - 20 um
AC - no BFPA

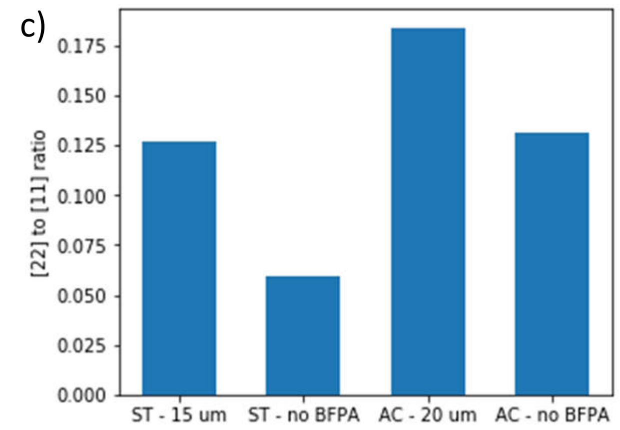
c)
[22] to [11] ratio
0.175
0.150
0.125
0.100
0.075
0.050
0.025
0.000
ST - 15 um
ST - no BFPA
AC - 20 um
AC - no BFPA

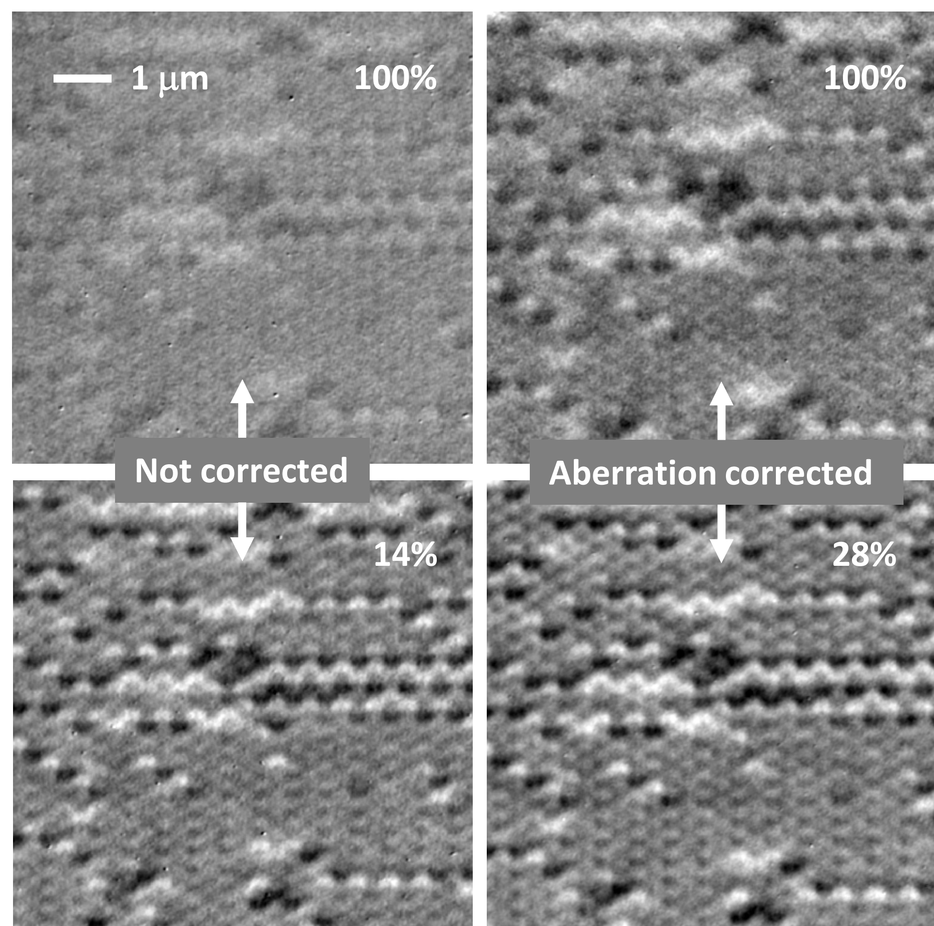
1 μm
100%
100%
Not corrected
Aberration corrected
14%
28%